Check for updates

Rice leaves microstructure-inspired high-efficiency electrodes for green hydrogen production†

Yuliang Li,‡[a] Jinxin Gao,‡[a] Zhaoyang Wang,[a] Honghao Li,[a] Lu Li,[a] Xiaofang Zhang,*[b] Xiaoyang Fan,[a] Longyun Lin,[a] Yan Li,[c] Ke Li,[a] Chunyu Zhang,[a] Linyang Li,[a] Ran Wang,[a] Yunting Su[a] and Dongliang Tian [ID] *[a]

Hydrogen production *via* water electrolysis is deemed a prime candidate for large-scale commercial green hydrogen generation. However, during the hydrogen evolution reaction (HER) and oxygen evolution reaction (OER), bubble accumulation on the electrode surface substantially elevates the required voltage and diminishes electrolysis efficiency. In this work, we demonstrated a rice leaves-inspired anisotropic microstructured gas conduction electrode (Ni-conduction) that can rapidly detach bubbles from the anisotropic microstructure. The microstructured grooves on the electrode surface lower the interface energy and modify bubble detachment dynamics, enabling swift bubble release and directed bubble flow along the microstructured channels. As a result, the Ni-conduction achieves a reduction in HER/OER overpotential, reaching values of 92/123 mV at 10 mA cm^{-2}. This performance significantly surpasses the performance of a flat nickel electrode (Ni-smooth), necessitating an overpotential of 183/176 mV under identical conditions. Furthermore, the assembled Ni-conduction||Ni-conduction overall water-splitting device only needs a cell voltage of 1.53 V to reach 10 mA cm^{-2}. Our research emphasizes the significance of wettability design in electrode microstructure to enhance mass transfer and optimize water splitting efficiency, presenting novel strategies for the development of superior gas-evolution electrodes.

Introduction

Water electrolysis has the potential to generate green hydrogen energy, thereby significantly contributing to the establishment of a near-zero emission society.[1–4] However, bubbles generated during the hydrogen evolution reaction (HER) and oxygen evolution reaction (OER) adhere to the electrode surface *in situ*, thereby diminishing the effective contact area between the electrode and the electrolyte.[5,6] This phenomenon results in a reduction of the active area available for the electrolytic reaction, consequently decreasing the efficiency of hydrogen production *via* water electrolysis.[7,8] As a result, the efficient removal of bubbles from the electrode surface during water electrolysis is essential to restore the effective active area, and

thus, it has emerged as a prominent area of research in recent years.[9–12]

The most widely adopted strategy to address this issue involves the construction of superhydrophilic electrode surfaces.[13,14] Bubbles are unable to adhere to such surfaces and detach from the electrode after undergoing nucleation and growth to a sufficient size, thereby minimizing their influence on the electrode reaction.[15,16] Currently, significant attention is directed towards the development of superwetting nanostructures, including nanosheets,[17,18] nanocones,[19] nanowires,[20,21] and nanoporous,[22] which have demonstrated promising applications in the field of water electrolysis. Furthermore, designing electrodes that utilize wettability gradients or shape gradients[23–25] to leverage the resultant Laplace pressure differences is a predominant approach to facilitate the directional motion of fluids.[26–29] Under an asymmetric wettability gradient, the generated bubbles undergo deformation, inducing a Laplace pressure that serves as a driving force for the directional movement of the three-phase boundary, thereby enhancing the detachment of the bubbles.[28,30,31] However, only a few related methods have been explored for gases transported over long distances on aerophobic surfaces.

Lots of biological surfaces demonstrate unique micro/nanostructures that control droplet dynamics. Inspired by this, these nature-based design strategies were applied to design

aKey Laboratory of Bio-Inspired Smart Interfacial Science and Technology, School of Chemistry, Beihang University, Beijing 100191, P. R. China.
E-mail: tiandl@buaa.edu.cn
bSchool of Mathematics and Physics, University of Science & Technology Beijing, Beijing 100083, P. R. China. E-mail: xfzhang926@ustb.edu.cn
cState Key Laboratory of Nonlinear Mechanics, Beijing Key Laboratory of Engineered Construction and Mechanobiology, Institute of Mechanics, Chinese Academy of Sciences, Beijing 100190, P. R. China
†Electronic supplementary information (ESI) available. See DOI: https://doi.org/10.1039/d4nr05151c
‡These authors contributed equally to this work.

wettable materials that achieve precise control of fluid behaviors.[32–34] For example, rice leaves have microscale structures that can arrange themselves in an orientation promoting anisotropic water droplet movement.[35] Inspired by the anisotropic wetting characteristics of rice leaves' surface, a high-efficiency electrode for hydrogen production *via* water electrolysis was developed. This electrode integrates wettability and morphological design *via* laser etching and electrodeposition; this design enhances bubble conveyance. The resultant anisotropic microstructured gas conduction electrode (Ni-conduction) facilitates the *in situ* collection and directed transport of H_2 and O_2 that are produced during the electrolysis process. Ni-conduction achieves HER/OER overpotential of 92/123 mV at 10 mA cm^{-2}, which is a considerable decrease from the overpotential of a traditional flat nickel electrode (Ni-smooth) of 183/176 mV at 10 mA cm^{-2}. Utilizing Ni-conduction as a bifunctional electrode for overall water splitting, the system operates at a low potential of 1.53 V at 10 mA cm^{-2}. This novel approach acts as a universal design concept for multiphase catalytic systems; therefore, it has the potential to be applied broadly to various gas evolution reactions.

Experimental section

Materials

$CuSO_4 \cdot 5H_2O$, $NaH_2PO_2 \cdot H_2O$, $Fe(NO_3)_3 \cdot 9H_2O$, and $Ni(NO_3)_2 \cdot 6H_2O$ were purchased from Alfa Aesar. Nickel metal with 99.9% purity and a thickness of 1 mm was used. All solutions in the present research were prepared with deionized water.

Synthesis of Ni-conduction

The femtosecond laser method was employed to fabricate various groove-containing Ni metal structures with ridge and groove microfeatures. A beam from a high-repetition-rate femtosecond laser system (Inngu Grace X 355-5) operating at 30 kHz and 1060 nm was utilized for the fabrication process. The laser power, scan pitch, and speed were set to 10 W, 50 μm, and 15 000 mm s^{-1}, respectively. The Ni-conduction electrode, featuring NiCuFeP nanoarray structure, was prepared on the groove Ni metal substrate *via* electrodeposition. Prior to electrodeposition, the groove Ni metal was cleaned with HCl and deionized water, followed by being sonicated for 5 min. The electrodeposition process was carried out using chronopotentiometry at −1.2 V for 1000 s. This process took place in a three-electrode setup at 25 °C, with the Ni-conducting serving as the working electrode, Hg/HgO as the reference electrode, and graphite as the counter electrode. The electrolyte solutions comprised 0.03 mmol $CuSO_4 \cdot 5H_2O$, 0.02 mmol $NaH_2PO_2 \cdot H_2O$, 0.03 mmol $Ni(NO_3)_2 \cdot 6H_2O$, and 0.02 mmol $Fe(NO_3)_3 \cdot 9H_2O$. After electrodeposition, the electrode was rinsed with water and allowed to dry at room temperature.

Synthesis of Ni-smooth

The Ni metal surface was subjected to treatment with HCl and deionized water, undergoing sonication for 5 min. Ni-smooth was subsequently prepared on the flat Ni metal surface, utilizing the same electrodeposition parameters.

Material characterizations

Scanning electron microscopy (SEM, CIQTEK Co., Ltd, SEM5000) was employed to examine the prepared samples. X-ray diffraction (XRD) patterns were captured using a Shimadzu XRD-6000 instrument at a scanning rate of 5° per minute. Contact angles of water (5 μL) and underwater bubbles (5 μL) were determined using a contact angle meter (SCI4000) at ambient temperature. The adherence forces of bubbles were quantified with a sensitive microelectromechanical balance system (SCI300M). In this process, a bubble (5 μL) was suspended with a copper loop and brought into contact with the sample at a constant speed of 0.005 mm s^{-1}. It was then retracted at the same speed. The detachment dynamics of underwater bubbles on the electrode surface were documented using a high-speed camera (Revealer 2F01M). Furthermore, the three-dimensional topography of the electrode surface was analyzed with super-high magnification lens zoom 3D microscopy (VHX-5000, Japan).

Results and discussion

In electrolytic water splitting, rapid desorption and transfer of bubbles are necessary to achieve high efficiency. Design an electrolytic water-to-hydrogen electrode by taking cues from the anisotropic rolling characteristics of rice leaves can help effectively direct bubbles away from the electrode surface by integrating anisotropic microstructures and bubble buoyancy, as depicted in Fig. 1a. To emulate the micrometer-scale features of rice leaves (Fig. S1†) that confer anisotropy, an anisotropic microstructured gas conduction electrode (Ni-conduction) was fabricated using laser engraving on a Ni metal substrate and electrodeposition (Fig. S2†). Scanning electron microscopy (SEM) and optical microscope analyses revealed that the nickel electrode, which was processed with laser etching, adopted a 3D groove microstructure, where the grooves measured 200 μm in width and spacing, as displayed in Fig. 1b, c, and S3.† The electrode surface is attached with a 500 nm popcorn-like spherical NiFeCuP nanostructure that was obtained by electrodeposition, as shown in Fig. 1d and S4.† Three-dimensional microscope images revealed that the gas conduction electrode has a depth of approximately 120 μm, showcasing a consistently organized 3D groove pattern, as illustrated in Fig. 1e and S5.† Energy dispersive spectroscope (EDS) mapping analysis depicted in Fig. 1f, S7, and S8† elucidate a homogeneous distribution of elements, including Cu, Fe, Ni, and P, across both the Ni-conduction and the Ni-smooth electrodes. Additional X-ray diffraction (XRD) studies were conducted to ascertain the constituents of the Ni-smooth and Ni-conduction electrodes, as represented in Fig. 1g. The XRD spectra revealed clear diffraction peaks corresponding to the nickel phase, which are characteristic of the (111), (200), and (220) crystallographic planes at 44.9°,
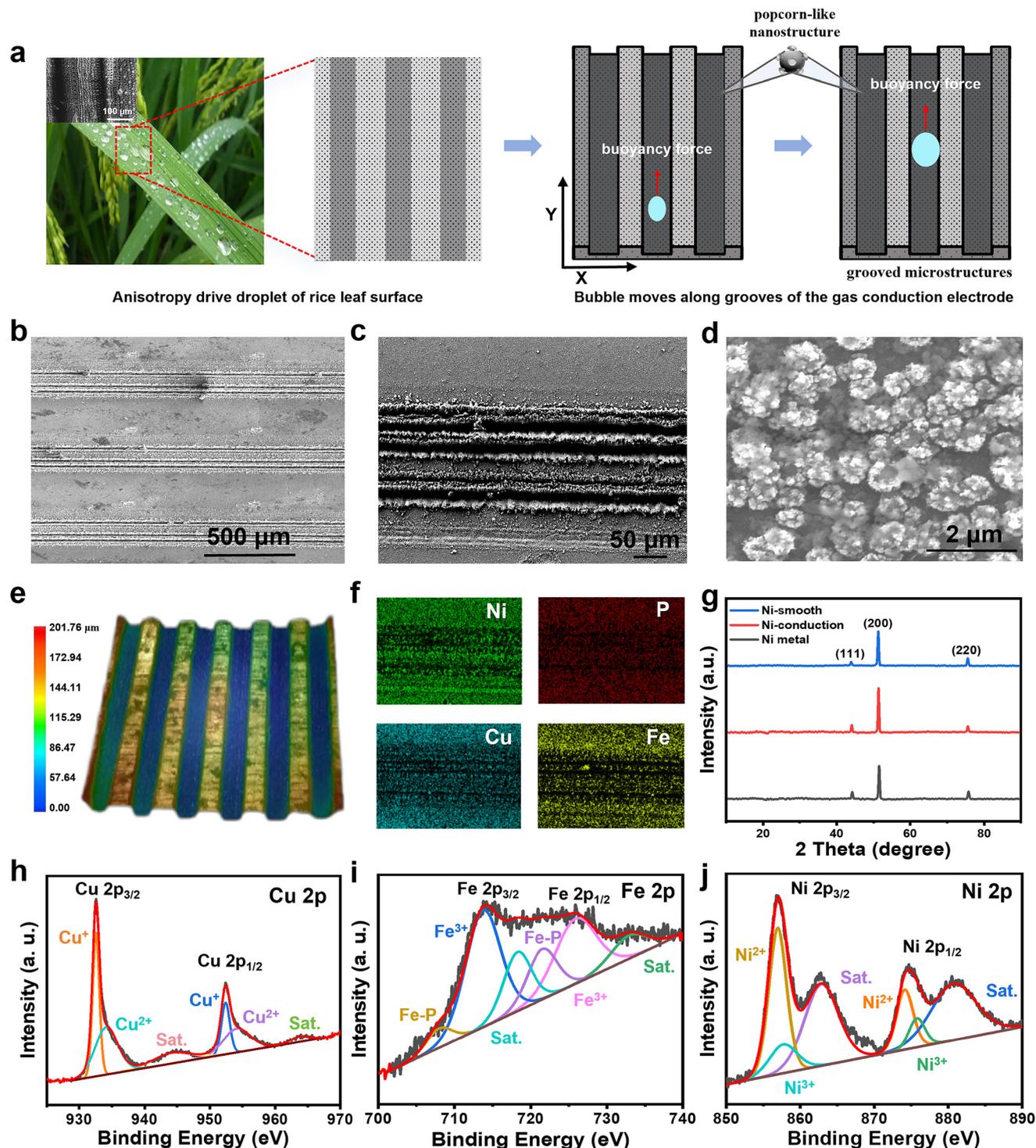
Fig. 1 Design concept and characteristics of anisotropic microstructured gas conduction electrode (Ni-conduction). (a) Inspiration from the aniso-tropic wetting microstructure of rice leaves to design a Ni-conduction electrode; the bubble moves on the Ni-conduction electrode, along with the grooves under buoyancy. The direction along the groove is *Y*, and the vertical groove direction is *X*. (b–d) SEM images of Ni-conduction at different magnification. (e) Three-dimensional microscope images of Ni-conduction. (f) EDS mapping images (Ni, P, Cu, and Fe) of Ni-conduction corres-ponding to (c). (g) XRD patterns of flat nickel electrode (Ni-smooth), Ni-conduction, and Ni metal substrate. High-resolution XPS spectra of Cu 2p (h), Fe 2p (i), and Ni 2p (j) for Ni-conduction.

52.1°, and 76.6°, respectively; these planes are consistent with the JCPDS No. 32-0306. To eliminate the influence of the Ni metal substrate, it was substituted with carbon paper.[36] As observed in Fig. S9,† the XRD profile of the NiFeCuP/carbon paper exhibited prominent peaks at 26.4° and 54.5° that were assignable to the (002) and (004) planes of graphite, with no additional peaks indicating the absence of crystalline phases. This suggests that the electrodeposition yielded a NiFeCuP layer in an amorphous state. The X-ray photoelectron spectroscopy (XPS) analysis of the Ni-conduction sample, as displayed in Fig. S10a,† validates the presence of pronounced peaks corresponding to Ni, Fe, Cu, and P elements. In the Cu 2p XPS spectrum (Fig. 1h), the Cu $2p_{3/2}$ region features a satellite peak at 944.1 eV, along with two distinct peaks at 932.5 eV and 934.1 eV, which are ascribed to Cu^+ and Cu^{2+} states, respectively. The Cu $2p_{1/2}$ region shows a satellite peak at 963.8 eV, with additional peaks for Cu^+ and Cu^{2+} situated at 952.4 eV and 954.1 eV, respectively.[37] Fig. 1i illustrates that the peaks at 707.9 eV and 721.5 eV are predominantly due to the Fe–P (Fe 2p) bonding in NiFeCuP, whereas the peaks at 713.7 eV and 725.8 eV correspond to the Fe $2p_{3/2}$ and Fe 2p1/2 of Fe^{3+}, respectively. Accompanying satellite peaks at 718.2 eV and 732.8 eV were also observed.[38,39] The Ni 2p spectrum, as shown in Fig. 1j, comprises two spin–orbit doublets that are characteristic of Ni $2p_{3/2}$ (Ni^{2+} and Ni^{3+} states at 856.9 and 857.6 eV) and Ni $2p_{1/2}$ (Ni^{2+} and Ni^{3+} states at 874.1 and 875.7 eV), respectively, along with a satellite peak at 862.8 eV and 880.6 eV.[40,41] Fig. S10b† presents the high-resolution P 2p spectrum, consisting of a doublet for the P $2p_{3/2}$ component at 129.4 eV and the P $2p_{1/2}$ component at 131.4 eV. This doublet originates from transition metal phosphides, while a distinct peak at 133.6 eV aligns with the phosphate species (P–O).[42]

The wettability of the fabricated electrodes was assessed through static contact angle measurements, as shown in Fig. 2a and Fig. S11.† The Ni-conduction electrode demonstrated distinct anisotropic wetting behavior compared to the Ni-smooth electrode, as evidenced by the variation in the static contact angles of droplets and bubbles, along the groove's orientation (Y-direction) and perpendicular to it (X-direction). The droplet (5 μL) contact angles (CA) in the air along the Y-direction Ni-conduction, X-direction Ni-conduction, and Ni-smooth were determined to be 27°, 82°, and 24°, respectively. In comparison, the underwater bubble (5 μL) CA recorded for the Ni-conduction in the Y-direction, the Ni-conduction in the X-direction, and the Ni-smooth electrode were 146°, 159°, and 108°, respectively, signifying their aerophobic properties. Significantly, in addition to featuring popcorn-like nanostructures, the Ni-conduction electrode, which had been laser-treated to form grooved microstructures, presented better superaerophobic properties as compared to the Ni-smooth counterpart. This phenomenon can be attributed to the discontinuity of the three-phase contact line between the bubbles and the electrode micro/nanostructure surface, leading to a significant decrease in the contact area between the bubbles and the electrode surface.[5] The superior properties of surface superaerophobicity and anisotropic wettability of the Ni-con-

duction electrode contribute to the rapid detachment of bubbles from the electrode surfaces during the gas evolution reaction. To gain insight into the differences in bubble detachment on the groove microstructured electrodes, we performed an analysis of the bubble adhesion force for Ni-smooth and Ni-conduction. Fig. 2b illustrates that at a compression distance of 0.5 mm, the Ni-conduction electrode exhibits a reduced adhesion force (Δ_{Force} = 3.13 μN) as compared to the Ni-smooth electrode (Δ_{Force} = 154.90 μN). This observation is consistent with the results shown in Fig. 2c and S12;† this is also illustrated by the variation in bubble attachment time in Fig. 2b inset. Drawing from these findings, we conducted a mechanistic investigation into the behavior of bubbles/droplets infiltrating the surfaces of the Ni-smooth and Ni-conduction electrodes. The Cassie–Baxter and Wenzel models are pivotal in correlating surface textures with the apparent CA of bubbles on a submerged solid surface. For rough hydrophilic surfaces, the apparent CA (θ_w^*) is directly proportional to both the intrinsic contact angle (θ) within the plane and the surface roughness factor (r), which captures the ratio of the real contact area to the projected area.[13]

$$\cos \theta_w^* = r \cos \theta \quad (1)$$

Therefore, as the surface roughness of the electrode increases, the θ_w^* value increases accordingly, thus facilitating the transition from the hydrophilic to the superhydrophilic state (Fig. $2d_1$ and e_1). On the other hand, for intrinsically aerophobic surfaces, an enhancement in the surface roughness also induces a superaerophobic condition, as shown in Fig. $2d_2$ and e_2.[43] In this superaerophobic state, minimal bubble contact occurs with the roughened surface, creating a liquid gap. Under such circumstances, the Cassie–Baxter model from eqn (2) provides the appropriate theoretical framework for analysis.[5]

$$\cos \theta_{CB}^* = f_s(\cos \theta + 1) - 1, \quad (2)$$

where f_s and θ_{CB}^* are the partial contact areas, and CA is the Cassie–Baxter state. Furthermore, the interaction between the droplet/bubble contact plane and the microstructure surface was examined using finite element analysis. Droplets could spread more effectively over a microstructured surface than over a flat one, as shown in Fig. $2d_3$ and e_3. For bubbles, the microstructure is more aerophobic than the flat structure, and its surface energy is very low. Therefore, bubbles are not allowed to be adsorbed on the surface.[44] Upon contacting the groove microstructure, bubbles exhibit a dynamic spread-contract behavior due to momentum, as depicted in Fig. $2d_4$ and e_4. This dynamic interaction allows easy bubble detachment from the surface – this feature is typical of superaerophobic materials that are characterized by the presence of discontinuous three-phase contact lines. A 50 μL bubble slides along the surface of the Ni-conduction electrode at 8° inclination, where the primary impetus propelling the bubble is the buoyancy-driven force (F_d) acting along the grooves. Conversely, the resistance encountered by the bubble as it moves along the grooves
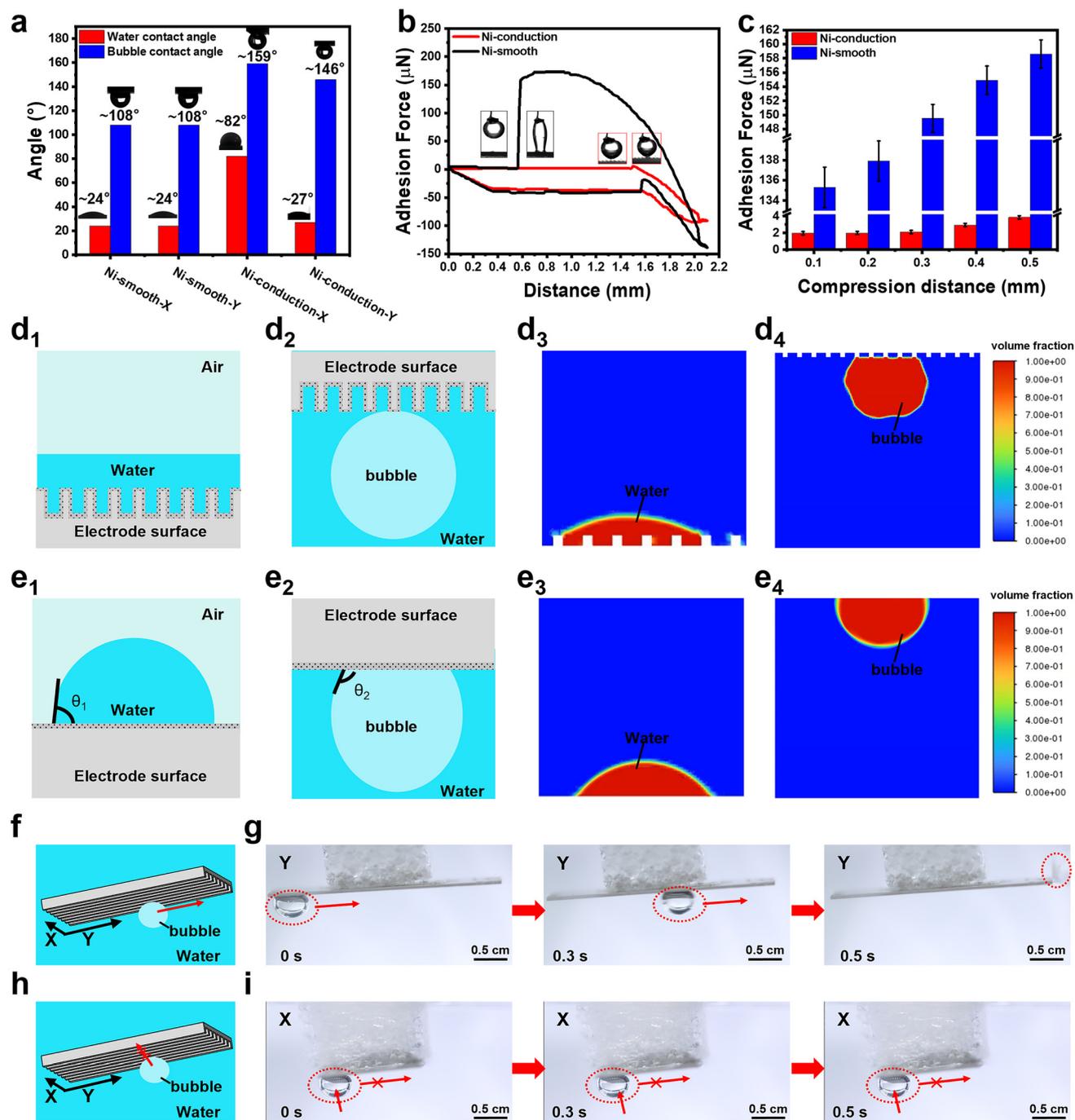
Fig. 2 Wettability characterization and finite element simulation of Ni-smooth and Ni-conduction electrode. (a) Contact angle of drop (5 μL) and bubble (5 μL) on Ni-smooth and Ni-conduction. (b) Bubble (5 μL) adhesion test with Ni-smooth and Ni-conduction. (c) Adhesion test of Ni-smooth and Ni-conduction at different compression distances. (d_1 and d_2) Contact relationship between droplets and bubbles on Ni-conduction surface and (d_3 and d_4) finite element simulation. (e_1 and e_2) Contact relationship between droplets and bubbles on Ni-smooth surface and (e_3 and e_4) finite element simulation. In the Y-direction, bubbles can be detached from the Ni-conduction electrode surface at an 8° angle, related schematic (f) and photographic (g) images. In the X-direction, the bubble cannot be detached from the Ni-conduction electrode surface at an 8° angle, related schematic (h) and the photographic (i) images.

is attributed to the CA hysteresis (F_{CAH}).[45] In the Y-direction, the resistance offered by F_{CAH} is less than F_d (6.6×10^{-5} N < 6.82×10^{-5} N), allowing the bubble to glide effortlessly along the groove as the bevel angle reaches 8° (Fig. 2f and g). In con-

trast, along the X-direction, the F_{CAH} is greater than F_d (18.2×10^{-5} N > 6.82×10^{-5} N), preventing the bubble from sliding (Fig. 2h and i) at the same angle, and the bubble needs an angle of 24° to slide. For the Ni-smooth surface at the same

bevel angle, the F_d of the 50 μL bubbles was insufficient to overcome the F_{CAH} in either direction, thus the bubbles remained stationary (Fig. S13 and Table S1†).

The performance of the alkaline HER/OER on the electrodes was evaluated by using Ni-conduction and Ni-smooth electrodes as the working electrodes in a three-electrode system immersed in 1.0 M KOH solution, as shown in Fig. 3a. The polarization curves for both Ni-conduction and Ni-smooth electrodes are shown in Fig. 3b, with iR compensation applied. The HER performance of Ni-conduction and Ni-smooth electrodes are characterized by HER overpotentials of 92 mV and 183 mV at current densities of 10 mA cm^{-2}. To delve deeper

into the HER kinetics in an alkaline environment, Tafel slopes were determined to gain insight into the catalytic mechanisms and reaction pathways involved. Fig. 3c illustrates the Tafel plots for the respective electrodes, which were derived from the polarization curve data. The Tafel slopes calculated for Ni-conduction and Ni-smooth electrodes are 78 and 98 mV dec^{-1}, respectively. Notably, the Tafel slope for Ni-conduction lies within the typical range of 120 to 40 mV dec^{-1}, suggesting that the HER kinetics for Ni-conduction are governed by the Volmer–Heyrovsky mechanism.[46,47] The i–t curves (Fig. S14a†) recorded in an alkaline medium reveal that Ni-conduction can sustain continuous operation for 30 hours without experien-
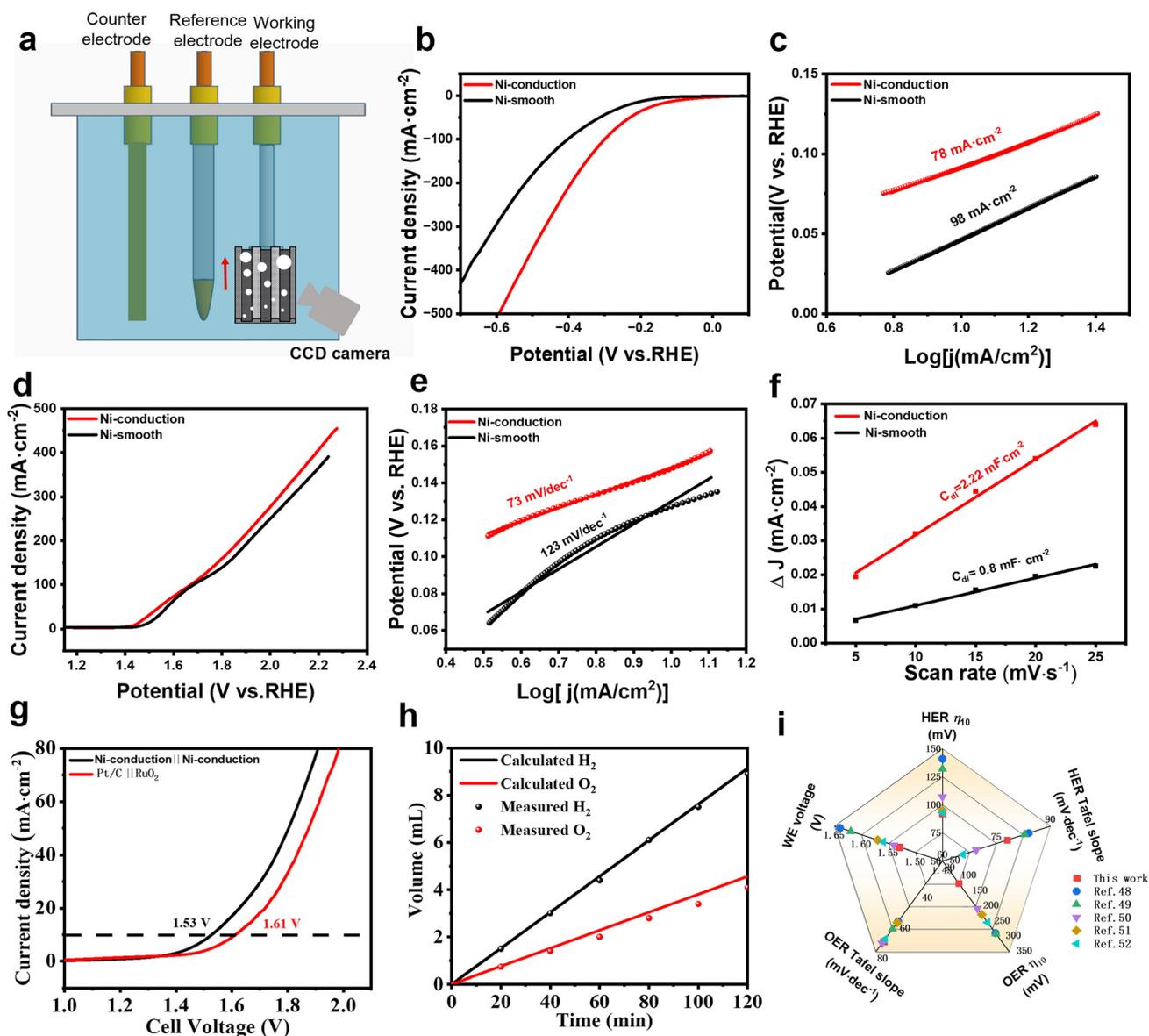

Fig. 3 Electrochemical water splitting performances test. (a) Diagram of a three-electrode electrolytic cell for electrolysis of water. (b) HER linear sweep voltammetry (LSV) curves of Ni-smooth and Ni-conduction in 1.0 M KOH. (c) Corresponding HER Tafel diagram. (d) OER LSV curves of Ni-smooth and Ni-conduction in 1.0 M KOH. (e) Corresponding OER Tafel diagram. (f) Double-layer capacitances of the prepared electrodes. (g) Polarization curves of the prepared electrodes for overall water splitting in the two-electrode configuration. (h) Calculated and measured volumes for H$_2$ and O$_2$. (i) Electrochemical water splitting performances of Ni-conduction comparison with the different electrodes.

cing significant performance deterioration. Following 5000 cyclic voltammetry (CV) scanning, the polarization curve of the Ni-conduction electrode for HER demonstrates minimal variation (Fig. S15a†). This electrochemical stability suggests that the Ni-conduction electrode possesses remarkable durability under prolonged operational conditions.

Electrocatalytic OER performances were assessed to further elucidate the enhancement in the electrochemical performance in groove microstructure. The OER performance of Ni-conduction, requiring an overpotential of 123 mV to achieve a current density of 10 mA cm^{-2}, was notably superior to that of Ni-smooth (176 mV) and commercial RuO$_2$ (250 mV), as shown in Fig. 3d and S16b.† To further probe the kinetic processes involved in the alkaline OER of the Ni-conduction electrode, Tafel plots for the different electrodes were generated and are presented in Fig. 3e. These plots revealed that the Tafel slope for Ni-conduction (73 mV dec^{-1}) was more favorable than that for Ni-smooth (123 mV dec^{-1}) electrode, thereby affirming the enhanced OER kinetics associated with the former. Moreover, the i–t measurements suggest that the Ni-conduction electrode maintains its stable catalytic activity for over 30 hours (Fig. S14b†), with polarization curves analysis showing minimal shift after 5000 cycles (Fig. S15b†). The graphical representation in Fig. S17† of the electrodes' Nyquist plots reveals a decrease in the charge transfer resistance (R_{ct}) for Ni-conduction compared to the Ni-smooth electrode, signifying that the former exhibits superior electron transfer capabilities relative to Ni-smooth. To gain deeper insights into the superior electrochemical performance of Ni-conduction, it is crucial to assess the electrochemically active surface area (ECSA) of the electrode material. Utilizing CV with varying scan rates enables the measurement of CV curves for the electrodes (Fig. S18†), which in turn, enables the determination of the electric double-layer capacitance (C_{dl}). This capacitance is an indicator of the electrochemical surface area. As shown in Fig. 3f, the C_{dl} values for Ni-conduction and Ni-smooth are 2.22 mF cm^{-2} and 0.8 mF cm^{-2}, respectively, highlighting a significantly larger active surface area for Ni-conduction compared to Ni-smooth.

The water-splitting capabilities of the bifunctional Ni-conduction electrode were investigated further, leveraging its outstanding catalytic activity for the overall water-splitting process. Fig. 3g shows that the cell voltage required for the Ni-conduction electrode to reach a current density of 10 mA cm^{-2} in a 1.0 M KOH electrolyte at room temperature; this is impressively low at 1.53 V, which is less than the voltage needed by 20% wt Pt/C-RuO$_2$ electrode (1.61 V). Moreover, an exhaustive analysis was conducted to assess the energy efficiency of the Ni-conduction electrode in the context of the entire water-splitting reaction. The production volumes of O$_2$ and H$_2$ were meticulously documented at specified intervals throughout the procedure. The generated O$_2$ to H$_2$ ratio was found to be nearly 1 : 2, as illustrated in Fig. 3h. Moreover, the Faraday efficiency for H$_2$ generation in 1.0 M KOH solution with the Ni-conduction was greater than 95% (Fig. S19†), demonstrating the high energy conversion efficiency of the Ni-

conduction electrode-based system. The electrochemical water splitting performances of the Ni-conduction electrode surpasses that of some non-precious metal alkaline electrolytic water splitting electrodes (Fig. 3i and S20; Table S2†).[48-52] Additionally, the Ni-conduction electrode exhibited stable electrolysis in 1.0 M KOH for 30 hours at room temperature, maintaining a current density of 10 mA cm^{-2} and achieving an electrolytic stability of 98.5% (Fig. S21†). To investigate the structural evolution of the Ni-conduction electrode during the electrochemical process, comprehensive characterization was performed after 30 hours of HER and OER stability tests. As presented in Fig. S22 and S23,† both the SEM images and XRD patterns indicated negligible morphological alterations and phase transformations, confirming the excellent electrochemical stability of the Ni-conduction electrode. These findings are consistent with previous reports on transition-metal phosphides, which have demonstrated similar structural robustness under prolonged HER and OER stability tests.[39,53,54] These findings point toward the superwetting groove microstructure of the Ni-conduction electrode as a key factor in enhancing its electrochemical performance for both HER and OER.

During an electrochemical reaction, the accumulation of bubbles on the electrode surface leads to a reduction in the active surface area, which in turn, impacts the electrochemical activity. The overpotential loss (η) experienced by an electrode is significantly influenced by the formation of bubbles at the electrode–electrolyte interface during the process of water electrolysis:[55]

$$\eta = \eta_{act} + \eta_{ohm} + \eta_{con}, \tag{3}$$

where η_{act}, η_{con}, and η_{ohm} are activation overpotential, concentration overpotential, and ohmic overpotential. The η_{act} is commonly associated with the energy losses that occur during the electrochemical reactions at the electrode surface; the dynamics of bubble adhesion and detachment determine the value of η_{act}, serving as a crucial indicator to assess the electrochemical performance of an electrode. The behavior of hydrogen bubbles on the surface of the prepared electrodes was monitored *in situ* using a high-speed camera under a steady current of −10 mA cm^{-2} (Video S1†). Fig. 4a reveals that as compared to the Ni-smooth electrode (Fig. 4b), the Ni-conduction electrode facilitates the efficient detachment of gas bubbles, thereby reducing their residence time. Moreover, the groove microstructured substrate effectively constrains bubble size, leading to a more consistent distribution of hydrogen bubbles and expediting their removal. The Ni-conduction electrode proved to be highly effective in curbing bubble diameters to a mere 50 μm (Fig. 4c$_1$); the release of these bubbles occurred predominantly within 100 ms (Fig. S24†). On the other hand, the Ni-smooth electrode yielded a markedly larger average bubble diameter, clocking in at around 560 μm, with a size distribution that ranged broadly up to 640 μm (Fig. 4c$_2$). Bubble detachment from Ni-smooth was largely delayed, with a concentration at approximately 2600 ms (Fig. S24b†). The findings imply that Ni-conduction is adept at controlling the
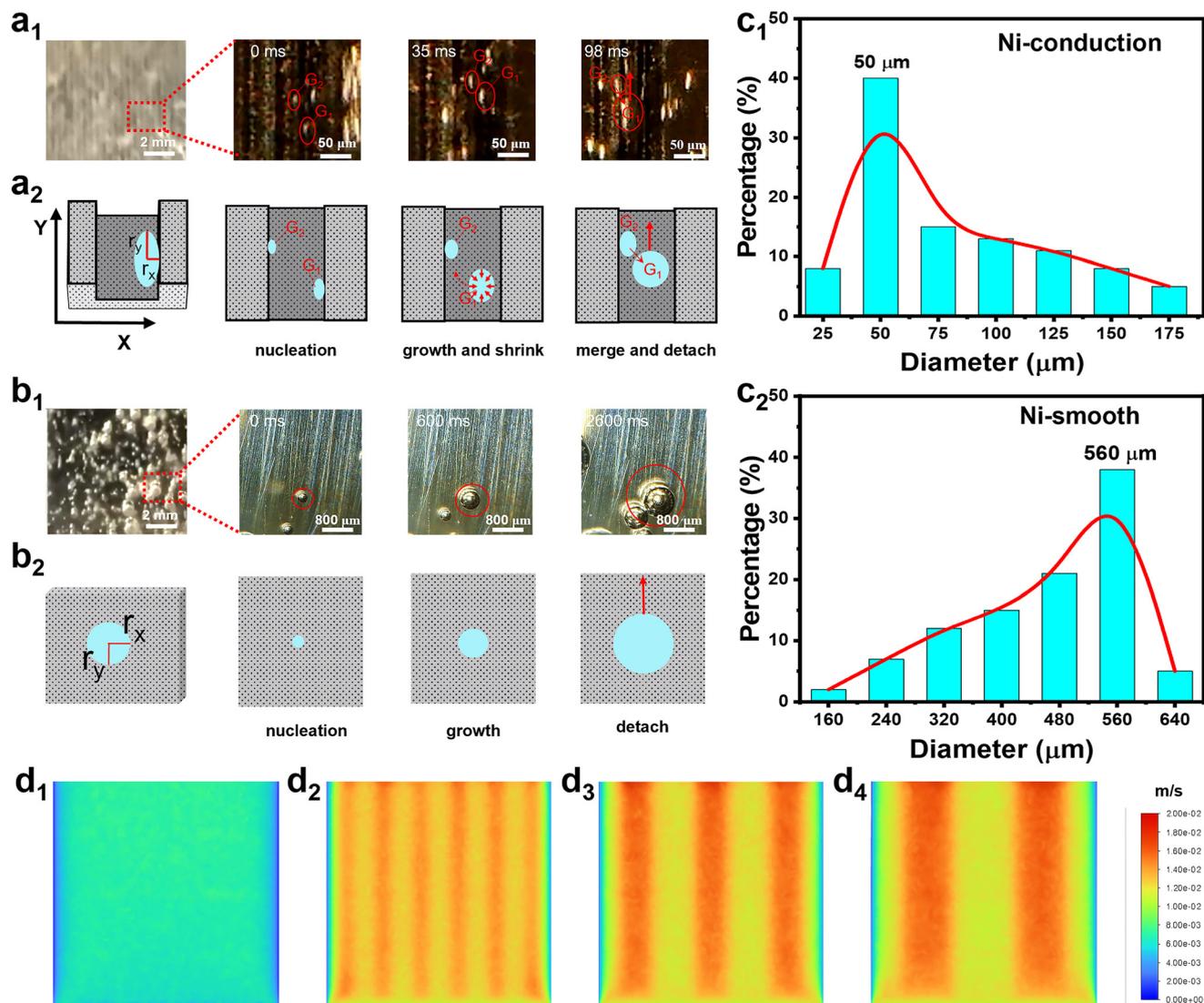
Fig. 4 Bubble evolution mechanism of Ni-conduction electrode during the electrolysis of water. The bubble G_1 (first *in situ* growth) and G_2 (later *in situ* growth) that grow between the ridge and the groove; G_1 floats and fuses with G_2 after desorption to achieve co-desorption at Ni-conduction (a_1). Bubbles grow and detach in place during the process on Ni-smooth (b_1). Bubble evolution mechanism of Ni-conduction (a_2) and Ni-smooth (b_2). r_x, r_y are the radii of the plane where the section of the bubble surface intersects in the *X* and *Y* directions. Bubble separation volume distribution for Ni-conduction (c_1) and Ni-smooth (c_2) during the HER process. Gas velocity finite element simulation of Ni-smooth (d_1), and Ni-conduction with groove width and spacing of 0.1 mm (d_2), 0.2 mm (d_3), 0.3 mm (d_4).

formation of bubble sizes, with enhanced mass transfer efficiency for bubble separation and ionic transmission. Our study shows that the incidence of bubble fusion is significantly higher during bubble formation on the Ni-conduction electrode, and the bubbles are rapidly separated along the fluted microstructure substrate after fusion. When bubble nucleation occurs at the boundary of a ridge and a groove, elliptical bubbles are formed during the initial growth stage, accelerating the nucleation, growth, and merger of bubbles. This phenomenon can be explained by Laplace's equation:[56]

$$\Delta P = \gamma \left(\frac{1}{r_x} + \frac{1}{r_y} \right), \quad (4)$$

where ΔP is surface pressure; γ is the unit interface force of water, and r_x, r_y is the radius of the plane where the section of the bubble surface intersects in the *X* and *Y* directions. For an ellipsoidal bubble, the internal pressure is different due to the different ambient partial pressures at the top (P_{upper}) and bottom of the bubble (P_{bottom}):

$$P_{upper} = \rho g h + P_{atm} + \Delta P, \quad (5)$$

$$P_{bottom} = \rho g (h + 2r_y) + P_{atm} + \Delta P, \quad (6)$$

where ρ is liquid density; g is the acceleration; h is depth at the top of the bubble, and P_{atm} is atmospheric pressure. However, due to its surface energy action, the bubble must shrink into a

sphere to achieve the minimum surface energy. Its interfacial force was γ_{shrink}:

$$\gamma_{\text{shrink}} = \gamma_{\text{l–g}} - \gamma_{\text{g–s}} + \gamma_{\text{g–l}} \cos \theta, \qquad (7)$$

where $\gamma_{\text{l–s}}$ is solid–liquid interfacial tension; $\gamma_{\text{g–s}}$ is gas–solid interfacial tension; $\gamma_{\text{g–l}}$ is gas–liquid interfacial tension, and θ is the bubble contact angle. The combined upward force ($F_{\text{ellipsoid}}$) of the external buoyant forces acting on the bubble is:

$$F_{\text{ellipsoid}} = \rho \frac{4}{3}\pi r_x{}^2 r_y g - \rho g h 2 r_y S + \gamma_{\text{shrink}} L + F_{\text{adhesion}}, \qquad (8)$$

where both S and L are the work area and distance traveled by the bubble to form a spherical bubble after normalization of the bubble. This results in violent perturbation of the bubble as it shrinks into a sphere, causing the bubble to detach. The force on the sphere is:

$$F_{\text{Sphere}} = \rho \frac{4}{3}\pi r_x{}^3 g + F_{\text{adhesion}}, \qquad (9)$$

The whole desorption process is as follows: take bubbles G_1 and G_2 for example, bubble G_1 first nucleates and grows to a certain scale. G_2 nucleates, and then G_1 floats up according to the above principles. G_2 grows *in situ*, and finally, G_1 and G_2 merge to achieve overall accelerated desorption (Fig. 4a). The adherence of bubbles to the Ni-smooth electrode is significantly higher compared to that on the Ni-conduction electrode (Fig. 4b). When a bubble detaches, it will float upward along the groove, and the top bubble will be fused by the detached bubble, which will greatly increase the buoyancy of the merged bubble, accelerating its detachment, driving its upward movement, reducing the desorption volume, and finally achieving fusion desorption (Fig. S25†). After bubble detachment, bubbles rise along the groove under the action of buoyancy and are close to the electrode surface, causing other growing bubbles to rise as well, as shown in Fig. S26.† As the upward force that aids bubble detachment is dependent on the bubble's volume, a considerable volume is necessary for a bubble to desorb from the surface of the Ni-smooth electrode. This may cause difficulty in detaching bubbles from the electrode surface. Furthermore, hydrogen flow rates (m s^{-1}) for different groove widths on the electrodes were visualized by further computational fluid dynamics (CFD) simulations for mass transfer comparisons (Fig. 4d). Compared to the microstructures, the gas flow rate on the planar surface is slower (Fig. 4d$_1$), and hydrogen can easily attach to the electrode surface, leading to active site occupation. In contrast, in the groove structures (Fig. 4d$_2$–d$_3$) hydrogen presents a uniform flow distribution when flowing in a flow-through mode. This groove structure allows the gas to form a linear path distribution at a stable velocity, reducing the diffusion of hydrogen into the active center. Notably, the structure with a groove width of 0.2 mm shows the fastest volumetric flow rate (Fig. 4d$_2$). Consequently, rice leaves inspired the development of an anisotropic microstructured Ni-conduction electrode, which facilitates anisotropic bubble transport across its surface. This design not only diminishes bubble adhesion to the electrode but also promotes the swift detachment of bubbles, thereby enhancing the electrochemical performances of the system.

Conclusions

In summary, we investigated the bubble dynamics on groove microstructured electrode surfaces that were inspired by bio-mimetic rice leaves through both experimental and theoretical means. This gas conduction nickel electrode is distinguished by its notable attributes: by preparing an anisotropic surface that is both hydrophilic and aerophobic, unique popcorn-like nanostructures and grooved microstructures were achieved that facilitate the formation of small volume bubbles that experience ready formation, conduction, and desorption. By constructing an anisotropic micro/nanostructure gas conduction nickel electrode surface, the adhesion force of bubbles on the electrode is reduced, while the anisotropic transfer behavior of bubbles on the electrode surface is guided by the synergistic effect of the micro/nanostructure and buoyancy force, making the bubbles detach from the electrode surface rapidly. Consequently, the Ni-conduction electrode has the HER/OER overpotential of 92/123 mV at 10 mA cm^{-2}, thereby substantially exceeding the performance of the Ni-smooth electrode that requires an overpotential of 183/176 mV under the same conditions. Moreover, the two-electrode electrolyzer with Ni-conduction requires only 1.53 V to achieve 10 mA cm^{-2}. Our findings demonstrate that engineering electrode wettability and architecture can enhance gas mass transfer, thereby elevating electrochemical performance. Our research establishes a theoretical framework to predict bubble behavior on wettable surfaces and paves the way for practical applications of wettable surfaces, such as in fluid transfer and water electrolysis processes.

Data availability

The data supporting this article have been included as part of the ESI.†

The methods, data, and analysis are described in sufficient detail within the manuscript to be reproduced.

Conflicts of interest

There are no conflicts to declare.

Acknowledgements

thank the assistance with SEM characterization at the Analysis and Testing Center of Beihang University, China.

References

1 G. Solomon, A. Landström, R. Mazzaro, M. Jugovac, P. Moras, E. Cattaruzza, V. Morandi, I. Concina and A. Vomiero, *Adv. Energy Mater.*, 2021, **11**, 2101324.

2 W. Liu, J. Yu, T. Li, S. Li, B. Ding, X. Guo, A. Cao, Q. Sha, D. Zhou, Y. Kuang and X. Sun, *Nat. Commun.*, 2024, **15**, 4712.

3 D. Friebel, M. W. Louie, M. Bajdich, K. E. Sanwald, Y. Cai, A. M. Wise, M.-J. Cheng, D. Sokaras, T.-C. Weng, R. Alonso-Mori, R. C. Davis, J. R. Bargar, J. K. Nørskov, A. Nilsson and A. T. Bell, *J. Am. Chem. Soc.*, 2015, **137**, 1305–1313.

4 Q. Zhao, Q. Zhang, Y. Xu, A. Han, H. He, H. Zheng, W. Zhang, H. Lei, U.-P. Apfel and R. Cao, *Angew. Chem., Int. Ed.*, 2024, **63**, e202414104.

5 W. Xu, Z. Lu, X. Sun, L. Jiang and X. Duan, *Acc. Chem. Res.*, 2018, **51**, 1590–1598.

6 P. A. Kempler, R. H. Coridan and L. Luo, *Chem. Rev.*, 2024, **124**, 10964–11007.

7 S. Park, L. Liu, Ç. Demirkır, O. van der Heijden, D. Lohse, D. Krug and M. T. M. Koper, *Nat. Chem.*, 2023, **15**, 1532–1540.

8 G. Liu, W. S. Y. Wong, M. Kraft, J. W. Ager, D. Vollmer and R. Xu, *Chem. Soc. Rev.*, 2021, **50**, 10674–10699.

9 Y. Li, N. Wang, H. Lei, X. Li, H. Zheng, H. Wang, W. Zhang and R. Cao, *Coord. Chem. Rev.*, 2021, **442**, 213996.

10 Z. Liu, Y. Du, R. Yu, M. Zheng, R. Hu, J. Wu, Y. Xia, Z. Zhuang and D. Wang, *Angew. Chem., Int. Ed.*, 2023, **62**, e202212653.

11 Y. Yan, Z. Guo, X. Zhang, L. He, Y. Li, K. Liu, J. Cai, D. Tian and L. Jiang, *Adv. Funct. Mater.*, 2018, **28**, 1800775.

12 J. R. Lake, S. Rufer, J. James, N. Pruyne, A. Scourtas, M. Schwarting, A. Ambadkar, I. Foster, B. Blaiszik and K. K. Varanasi, *Nanoscale*, 2025, **17**, 1270–1281.

13 M. Li, P. Xie, L. Yu, L. Luo and X. Sun, *ACS Nano*, 2023, **17**, 23299–23316.

14 Z. Lu, W. Zhu, X. Yu, H. Zhang, Y. Li, X. Sun, X. Wang, H. Wang, J. Wang, J. Luo, X. Lei and L. Jiang, *Adv. Mater.*, 2014, **26**, 2683–2687.

15 Y. Li, K. Li, L. Li, J. Gao, Z. Wang, W. Zou, H. Li, Q. Zhang, Y. Li, X. Zhang, D. Tian and L. Jiang, *Adv. Mater.*, 2024, **36**, 2405493.

16 L. Zhang, R. Iwata, Z. Lu, X. Wang, C. D. Díaz-Marín and Y. Zhong, *Chem. Rev.*, 2024, **124**, 10052–10111.

17 N. Han, K. R. Yang, Z. Lu, Y. Li, W. Xu, T. Gao, Z. Cai, Y. Zhang, V. S. Batista, W. Liu and X. Sun, *Nat. Commun.*, 2018, **9**, 924.

18 J. Kang, G. Liu, Q. Hu, Y. Huang, L.-M. Liu, L. Dong, G. Teobaldi and L. Guo, *J. Am. Chem. Soc.*, 2023, **145**, 25143–25149.

19 Q. Ren, L. Feng, C. Ye, X. Xue, D. Lin, S. Eisenberg, T. Kou, E. B. Duoss, C. Zhu and Y. Li, *Adv. Energy Mater.*, 2023, **13**, 2302073.

20 H. Shi, T. Wang, J. Liu, W. Chen, S. Li, J. Liang, S. Liu, X. Liu, Z. Cai, C. Wang, D. Su, Y. Huang, L. Elbaz and Q. Li, *Nat. Commun.*, 2023, **14**, 3934.

21 M. Xing, S. Zhu, X. Zeng, S. Wang, Z. Liu and D. Cao, *Adv. Energy Mater.*, 2023, **13**, 2302376.

22 S. Ding, Z. Li, G. Lin, L. Wang, A. Dong and L. Sun, *ACS Energy Lett.*, 2024, **9**, 3719–3726.

23 Z. Cui, Y. Shao, J. Zhang and Z. Wang, *J. Colloid Interface Sci.*, 2025, **682**, 629–642.

24 Z. Long, Y. Zhao, C. Zhang, Y. Zhang, C. Yu, Y. Wu, J. Ma, M. Cao and L. Jiang, *Adv. Mater.*, 2020, **32**, 1908099.

25 M. Cao, Y. Qiu, H. Bai, X. Wang, Z. Li, T. Zhao, Y. Tian, Y. Wu and L. Jiang, *Matter*, 2024, **7**, 3053–3068.

26 S. Zhang, M. Chi, J. Mo, T. Liu, Y. Liu, Q. Fu, J. Wang, B. Luo, Y. Qin, S. Wang and S. Nie, *Nat. Commun.*, 2022, **13**, 4168.

27 K. Li, Y. Li, Q. Zhang, H. Li, W. Zou, L. Li, Y. Li, X. Zhang, D. Tian and L. Jiang, *Mater. Horiz.*, 2025, **12**, 258–266.

28 J. Tan, Z. Fan, M. Zhou, T. Liu, S. Sun, G. Chen, Y. Song, Z. Wang and D. Jiang, *Adv. Mater.*, 2024, **36**, 2314346.

29 S. Feng, P. Zhu, H. Zheng, H. Zhan, C. Chen, J. Li, L. Wang, X. Yao, Y. Liu and Z. Wang, *Science*, 2021, **373**, 1344–1348.

30 Z. Long, C. Yu, M. Cao, J. Ma and L. Jiang, *Adv. Mater.*, 2024, **36**, 2312179.

31 C. Zhang, Z. Xu, N. Han, Y. Tian, T. Kallio, C. Yu and L. Jiang, *Sci. Adv.*, 2023, **9**, eadd6978.

32 Z. Wang, J. Zhang, Y. Shao, Z. Cui, Y. Zhao and Y. Zhang, *Sep. Purif. Technol.*, 2025, **360**, 130932.

33 Z. Wang, Y. Shao, T. Wang, J. Zhang, Z. Cui, J. Guo, S. Li and Y. Chen, *ACS Appl. Mater. Interfaces*, 2024, **16**, 15558–15568.

34 L. Li, Y. Li, K. Li, W. Zou, H. Li, Y. Li, L. Li, Q. Zhang, C. Zhang, X. Zhang, D. Tian and L. Jiang, *ACS Nano*, 2025, **19**, 1080–1089.

35 P. Li, M. Cao, H. Bai, T. Zhao, Y. Ning, X. Wang, K. Liu and L. Jiang, *Adv. Funct. Mater.*, 2019, **29**, 1904446.

36 L. Wan, Z. Xu, P. Wang, P.-F. Liu, Q. Xu and B. Wang, *Chem. Eng. J.*, 2022, **431**, 133942.

37 R. Andaveh, A. Sabour Rouhaghdam, A. Seif, K. Wang, M. Maleki, J. Ai, G. Barati Darband and J. Li, *ACS Appl. Mater. Interfaces*, 2024, **16**, 8717–8732.

38 J. Tong, Y. Li, L. Bo, W. Wang, T. Li and Q. Zhang, *Catalysts*, 2019, **9**, 692.

39 J. Ge, S. Diao, J. Jin, Y. Wang, X. Zhao, F. Zhang and X. Lei, *Inorg. Chem. Front.*, 2023, **10**, 3515–3524.

40 R.-Q. Li, B.-L. Wang, T. Gao, R. Zhang, C. Xu, X. Jiang, J. Zeng, Y. Bando, P. Hu, Y. Li and X.-B. Wang, *Nano Energy*, 2019, **58**, 870–876.

41 Z.-Y. Wu, W.-B. Ji, B.-C. Hu, H.-W. Liang, X.-X. Xu, Z.-L. Yu, B.-Y. Li and S.-H. Yu, *Nano Energy*, 2018, **51**, 286–293.

42 J. Wang, C. Chen, N. Cai, M. Wang, H. Li and F. Yu, *Nanoscale*, 2021, **13**, 1354–1363.

43 H. Bai, T. Zhao and M. Cao, *Chem. Soc. Rev.*, 2025, DOI: **10.1039/D4CS01073F**.

44 R. Xu, D. Zhu, K. Du, D. Cui, H. Feng, W. Hao, D. Tian and Y. Du, *Mater. Today Energy*, 2022, **25**, 100961.

45 C. Yu, X. Zhu, K. Li, M. Cao and L. Jiang, *Adv. Funct. Mater.*, 2017, **27**, 1701605.

46 N. Tuan Van, T. Mahider, L. Quyet Van, T. Chau Van, A. Sang Hyun and K. Soo Young, *Microstructures*, 2024, **4**, 2024046.

47 S. Li, E. Li, X. An, X. Hao, Z. Jiang and G. Guan, *Nanoscale*, 2021, **13**, 12788–12817.

48 J. Tong, Y. Li, L. Bo, W. Li, T. Li, Q. Zhang, D. Kong, H. Wang and C. Li, *ACS Sustainable Chem. Eng.*, 2019, **7**, 17432–17442.

49 X. Wang, J. Wang, J. Zhang, J. Wei, X. Tong, R. Xu and L. Yang, *J. Power Sources*, 2024, **621**, 235321.

50 T. L. Luyen Doan, D. T. Tran, D. C. Nguyen, H. Tuan Le, N. H. Kim and J. H. Lee, *Appl. Catal., B*, 2020, **261**, 118268.

51 F. Diao, W. Huang, G. Ctistis, H. Wackerbarth, Y. Yang, P. Si, J. Zhang, X. Xiao and C. Engelbrekt, *ACS Appl. Mater. Interfaces*, 2021, **13**, 23702–23713.

52 L. Yang, L. Huang, Y. Yao and L. Jiao, *Appl. Catal., B*, 2021, **282**, 119584.

53 X. Li, Z. Xie, S. Roy, L. Gao, J. Liu, B. Zhao, R. Wei, B. Tang, H. Wang, P. Ajayan and K. Tang, *Adv. Mater.*, 2024, 2410295, DOI: **10.1002/adma.202410295**.

54 J. Zhao, N. Liao and J. Luo, *J. Mater. Chem. A*, 2023, **11**, 9682–9690.

55 J. Yu, K. Hu, Z. Zhang, L. Luo, Y. Liu, D. Zhou, F. Wang, Y. Kuang, H. Xu, H. Li, H. Duan and X. Sun, *Energy Environ. Sci.*, 2023, **16**, 2068–2079.

56 Q. Zhang, X. Bai, Y. Li, X. Zhang, D. Tian and L. Jiang, *ACS Nano*, 2022, **16**, 16843–16852.